Simulated ocean circulation and its variability in the Northern Banda Sea from CROCO model

Amanda Dompeipen[1,*], *Apriansyah*[3], *Agus* Atmadipoera[2], *Nabil*[2], *Delta* Rumohoira[1], *Dwiyoga* Nugroho[4], *Nyoman* Natih[2], and *Yunita* Noya[5]

[1]Graduate Magister program in Marine Sciences, Faculty of Fisheries and Marine Sciences, IPB University, 16680, Bogor, Indonesia
[2]Marine Science and Technology Department, Faculty of Fisheries and Marine Sciences, IPB University, 16680, Bogor, Indonesia
[3]Marine Science Program, Faculty of Mathematics and Natural Sciences, Tanjungpura University, 78124, Pontianak, West Kalimantan, Indonesia
[4]Research Center for Oceanography, National Research and Innovation Agency, 10340, Central Jakarta, DKI Jakarta, Indonesia
[5]Marine Science Department, Faculty of Fisheries and Marine Science, Pattimura University, 97233, Ambon, Maluku, Indonesia

Abstract. A simulation of 1/24º resolution 3-dimension regional ocean circulation of CROCO was successfully performed from 2015 to 2022 (8 years), covering the ENSO year in El Niño 2015 and La Niña 2022 in the northern Banda Sea (NBS). The model and data comparison of sea surface temperature/height reproduced the observed satellite datasets well, with correlation coefficients above 0.9. It is shown that the mean circulation in the NBS is fed by two inflows from western Buru and the Manipa Strait, resulting in a meandering eastward mean circulation with warmer water accumulated in the eastern NBS, associated with high current variance south of Buru and along the Manipa Strait. Seasonal variations in the oceanographic parameters were dominant in the study area. For example, during the southeast (northwest) monsoon period, the seawater temperature is minimum (maximum) and the salinity is maximum (minimum). Furthermore, the interannual timescale ENSO and IOD significantly modulated seawater temperature and salinity variation, particularly at the thermocline layer (110 m). Much cooler and saltier water is associated with El Niño 2015 and a positive IOD, in contrast to warmer and fresher water during La Niña 2022 and a negative IOD.

1 Introduction

The Indonesian Maritime Continent (MC) is located in the tropics between the Pacific and Indian Oceans, and between the continents of Asia and Australia. MC's location of the MC makes its atmospheric and ocean interactions very complex in controlling regional and global atmospheric circulation. The global circulation of the atmosphere and ocean over the MC

* Corresponding author: amanda.dompeipen@gmail.com

region tends to result in high climatic variability. Global climate variability in the region. Global climate variability affecting the atmospheric and oceanographic conditions in Indonesia includes the El Niño Southern Oscillation (ENSO) and the Indian Ocean [1]. ENSO is a phenomenon that consists of two phases: a warm phase (El Niño) and a cold phase (La Niña). Southern Oscillation is a change in wind circulation caused by differences in sea surface temperature (SST) between the eastern and western Pacific [2]. This difference causes a reversal of atmospheric circulation over the oceans near the equator [3], resulting in global climate anomalies [4]. El Niño occurs when there is an increase in SST in the equatorial regions of the eastern and central Pacific, whereas La Niña is the opposite condition. During the El Niño period, there is a similar ENSO phenomenon in the Indian Ocean, commonly called the Indian Ocean Dipole (IOD). During the positive phase of the IOD, sea surface anomalies in the western Indian Ocean were warmer than normal, while those in the eastern Indian Ocean were cooler than normal.

The North Banda Sea is the deepest and largest basin-shaped water body in the Indonesian Sea (**Fig. 1**). These waters exhibit intricate water mass features because they are the intersection of the western path of the Indonesian Throughflow (ITF), with low salinity and cold features, from the Makassar Strait eastward into the Flores Sea, and the eastern ITF path, with warm features and higher salinity, from the Halmahera and Maluku Seas into the Seram Sea. The two water masses meet in the Banda Sea and exit the Indian Ocean through the Timor Gap and Ombai Strait [5,6]. These waters are also the paths of seasonal currents that occur twice a year [7,8]. The ITF is influenced by the dynamics of ocean-atmosphere interactions in the Pacific and Indian Oceans, such as the ENSO and IOD phenomena [8,9,10]. ENSO and IOD influence changes in SST and chlorophyll-a [11]. Therefore, it is necessary to determine the oceanographic parameters of the Banda Sea with ENSO and IOD climate variability.

Previous studies have investigated the influence of ENSO and IOD on the spatial distribution of SST and chlorophyll-a [12], the vertical structure and variability of the ITF flowing into the western edge of the Banda Sea [13], the horizontal structure of eddies in the Banda and their relationship to chlorophyll-a during the 2008-2010 southeast monsoon in normal and ENSO periods [14], ENSO-influenced ITF transport [15], changes in surface circulation patterns during the 2008/2009, 2009/2010, and 2010/2011 “normal” events with implications for the Ekman layer and upwelling intensity [16], and research on the relationship of ENSO and IOD to SST and chlorophyll-a in the Banda Sea and the southern coast of Java, concluding that these phenomena have an influence on SST and chlorophyll-a variability [17]. However, no one has studied the variance and variability of each oceanographic parameter, such as SST, seawater temperature, SSH, salinity, zonal, and meridional current components, and their relationship with ENSO and IOD phenomena with the time series until 2022. Therefore, this research can provide an overview of the ocean dynamics during the ENSO and IOD phenomena in the waters of the North Banda Sea, so that it can be used for monitoring and further studies.

2 Methods

2.1 Study area

The study area is located in the North Banda Sea, in the southern part of Buru Island, Ambon Island, Seram Island, and Lease Island. The Northern Banda Sea (125.5°–131.96°E and 3.22–6.5°S) was the area and domain model for this study (**Fig. 1**). As part of our analysis, we utilised the Banggai Upwelling Dynamics and Ecosystem Experiment (BUDEE) cruise data

to conduct a comparison between our observational and modelled data for two stations located within the study area.

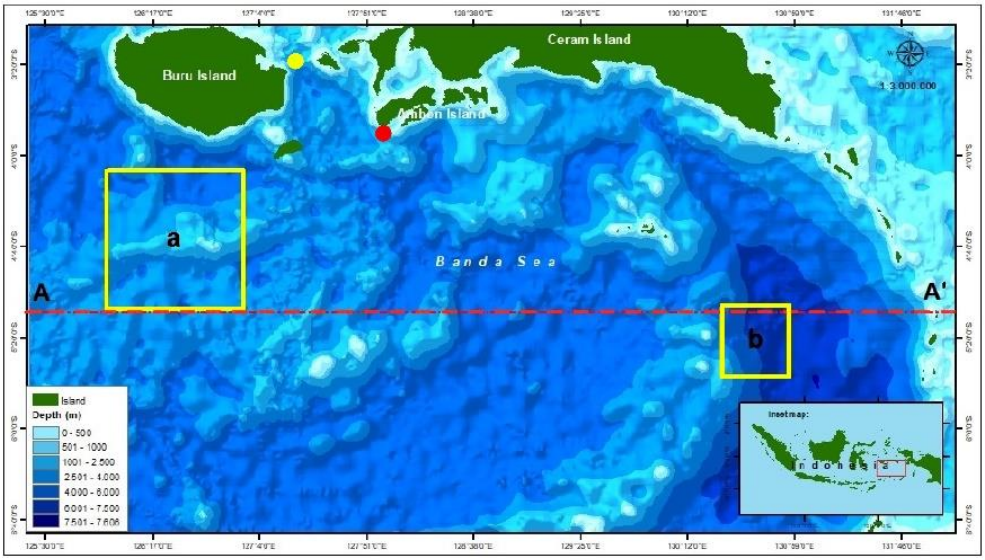

Fig. 1. Study area in the Northern Banda Sea. The sampling boxes for validation (yellow box) were divided into areas A and B for SST and SLA data. Red dashed lines are used for the Hovmoller analysis, and the observational data are depicted with red and yellow dots for stations 1 and 2, respectively.

2.2 Data

This study applied regional model configuration using the coastal and regional ocean community (CROCO) model version 3.0. The model area expands from 125.5°to 131.96°E and 3.22–6.5°S (**Fig. 1**). The model domain was established with spatial resolution of 1/24º and 50 vertical layers. The topography of the General Bathymetric Chart of the Oceans (GEBCO) gridded dataset was used to generate the bathymetric model for 15 second [18]. The slope parameter, which was 0.25, prevented horizontal pressure gradient errors [19].

The ROMS_TOOLS toolbox was used to apply the hydrodynamic model configuration [20]. Open boundaries were set up on the southern, eastern, and western sides of the model domain. Explicit tide forcing was obtained from the TPXO.9 dataset with a horizontal resolution of 1/6º [21]. The tidal constituents were used as open boundaries. The GLORYS12V1 reanalysis product was used to obtain the lateral boundary conditions [22], which had a horizontal resolution of 1/12º and a time span of 2015 to 2022. Atmospheric parameters, forcing the model, were obtained from ERA5 data at 1/4º horizontal resolution [23]. The model simulations ran from 1 January 2014 to 31 December 2022 where 2014 is a spin-up year with 3-dimension parameters as the output such as sea surface height, temperature, salinity, and current components (zonal and meridional).

Observational imagery from satellites was used to validate the model accuracy. Marine Copernicus (https://resources.marine.copernicus.eu/) provides satellite data for the sea surface temperature (SST) with a spatial resolution 0.05º and the sea surface height anomaly (SSHA) with a spatial resolution 0.24º, which were used to validate the output of the CROCO model. These datasets are global in scope and have a daily temporal resolution.

Additionally, this study compared the model and observational data collected during the BUDEE cruise at the same time and location. The analysed variables were temperature and salinity data collected by Conductivity, Temperature, and Depth (CTD) in September 2022 at Station 1 (127.96E, 3.80 °S) on 04 and Station 2 (127.33 °E, 3.33 °S) on 05.

2.3 Data analysis

The mean and variance from January 2015 to December 2022 were computed and visualised to demonstrate the greatest fluctuation in the model in the Northern Banda Sea (NBS). The investigation involved analysing and visualising the Hovmoller diagrams of temperature, salinity, and current components to determine their signal propagation along 5°S from the time-series data according to [24]. To compare certain parameters, time series data were extracted from the study area (**Fig. 1**) from 2015 to 2022. We also analysed the time series to show the temporal variability of certain oceanic parameters at different depths. Furthermore, the period of the time-series data was specified using the power spectral density (PSD), as described in [26]. Eddy kinetic energy (EKE) was also analyzed according to [33]. In addition, time series of interannual variations of oceanic parameters were used to analyse their relationship to El Niño Southern Oscillation (ENSO) indices obtained from the NOAA National Centers for Environmental Information Climate Monitoring (https://www.cpc.ncep.noaa.gov/) and Indian Ocean Dipole indices obtained from NOAA Physical Sciences Laboratory (https://psl.noaa.gov/).

2.4 Data validation

Plotting data from 2015 to 2022 from the sampling box area was used for validation (**Fig. 2a, 2b**). The output of the CROCO model was validated using satellite observations. According to [27], the Taylor diagram is a graphical analysis diagram that summarises the pattern of model estimation and observation matches, describing three statistical parameters: the root mean standard error (RMSE), correlation coefficient (r), and standard deviation between the model and observation. To determine the best-performing model, it is important to consider the correlation between variables, with a correlation of 1 indicating perfect correlation, as well as the RMS difference between the model and the data, with the highest correlation and lowest RMS difference being the ideal combination, and to ensure that the standard deviation of the model is similar to that of the observations [25]. Thus, the validation was performed using a Taylor Diagram to obtain the accuracy of the model, as shown in (**Fig. 2c**).

Fig. 2 shows the validation of the model data and satellite observations, with the black line representing the model and red line representing the satellites. After examining the validation results shown in **Fig. 2a** and **2b**, it is evident that the CROCO model is well suited for future research. The SST validation revealed a correlation coefficient of 0.8962, RMSE of 0.5571, and standard deviation of 1.1124. In addition, the SLA validation showed a correlation coefficient of 0.9139, RMSE of 0.0457, and standard deviation of 0.0836.

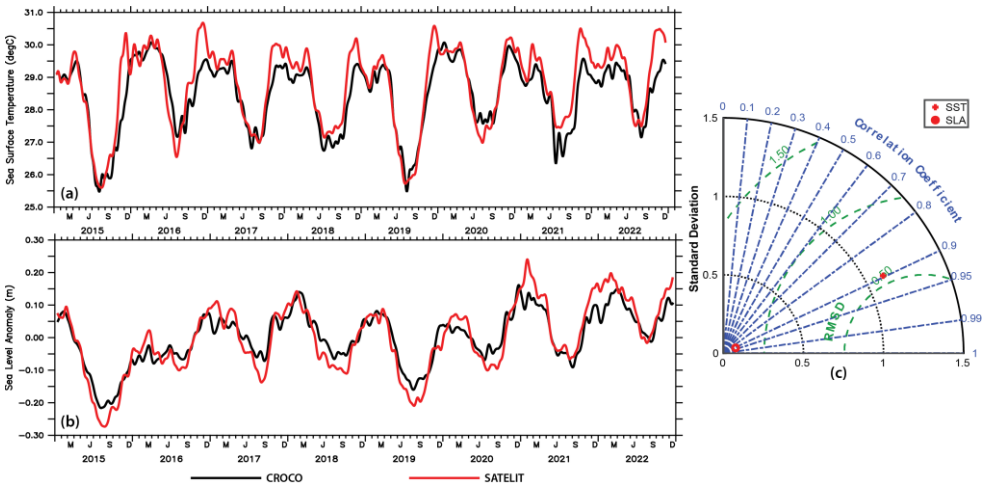

Fig. 2. Comparison of the model and satellite data of SST (a) and SLA (b) along with the Taylor diagram (c) in the study area.

3 Results and discussion

3.1 Vertical profiles of temperature and salinity from the model and observational data

A comparison between the CROCO model simulation data and cruise observation data (CTD) is shown in **Fig. 3**. The CROCO model data were extracted from the point closest to CTD station. The extracted data were matched to the time and depth of the observational data, ensuring that the two sets of data were aligned. At station 1 (**Fig. 3a**), the temperature in the surface layer was ~28°C. The temperature values of the model simulation and CTD show differences, with a maximum range of up to 7°C at a depth of 75 m, which then starts to remain constant until a depth of 400 m. Where the model data had the lowest temperature of 9.5 °C, the CTD was 10.18°C. The temperature profile overlay indicated a decrease in temperature with increasing depth. The surface layer had the highest temperature, whereas the thermocline layer had a significant decrease in temperature and was relatively homogeneous in the deep layer. Furthermore, at station 2, both the model and CTD data indicated a decrease in the sea surface temperature from 29°C with increasing depth. The thermocline layer is more clearly displayed in the CTD data at station 2, which is situated at a depth of 76 m, compared to station 1. While it is comparatively easier to determine the thermocline layer at station 1, station 2 is located at a depth of 66 m. The temperature at a depth of 1000 m, as per the CTD data, was 5.35°C. However, as per the model data extracted at a maximum depth of 968 m, the temperature reaches 4.67°C.

The vertical salinity profile at Station 1 shows that the surface salinities from the CTD data are lower than those from the model data, 33.53 psu and 34.91 psu, whereas the model data are higher. As the depth increased, the salinity values increased and ultimately stabilised at 111 m, with both datasets indicating a range of 34.5 psu. At station 2, the surface salinity values for the model and CTD data were 35 psu and 34.87 psu, respectively. Both datasets illustrate increasing homogeneity and constancy in salinity values from a depth of 229 meters, ranging from 34.57–34.59 psu, to 1000 meters.

The data presented in **Fig. 3** reveal notable differences between the subsurface layers. These differences may be attributed to the fact that the model configuration cannot be

extracted precisely at the CTD location, but only at the closest coordinates. Nonetheless, the overall model area can still be thoroughly examined based on previously conducted model validation data obtained from two significant areas.

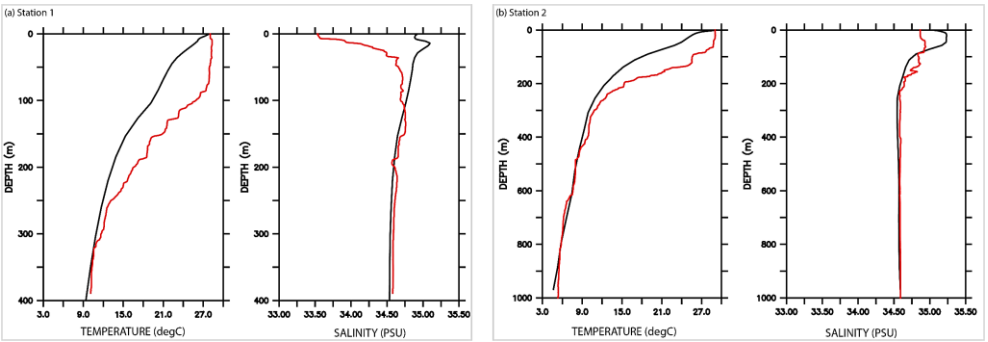

Fig. 3. Comparison between the CROCO model (black line) and CTD (red line). The locations of the CROCO data extraction were 127.962°E, 3.802°S (station 1) and 127.337°E, 3.345°S (station 2). The CTD locations were 127.958°E, 3.803°S (station 1), and 127.335°E and 3.325°S (station 2).

3.2 Mean and variance of the oceanographic parameters

Fig. 4 shows the mean and variance values of the temperature in the sea surface, near-surface, and thermocline layers in the NBS. Mean and variance are used to show the variability and dispersion of the distribution of ocean parameters, and their patterns can be related to dynamic mechanisms. **Fig. 4a** illustrates the range of mean sea surface temperature values, specifically 27–28.9°C for the sea surface layer, 23.5-25.5°C for the near-surface layer, and 16–19.4°C for the thermocline layer. The temperature in the surface layer of the Banda Sea is relatively warm, with an average of 28.4°C. In the Banda Sea arc section, the temperature is further increased to 28.7°C and >28.8°C in the western part of the Banda Sea arc section. This is in agreement with [28], which states that the surface temperature of the Banda Sea has a range of 26–30°C. The near-surface layer displays a variable temperature distribution, with temperatures near the island cooler than those offshore. Furthermore, higher temperatures form the Banda Sea arc, with a maximum temperature of 26.5°C. The western part of the Banda Sea had a similar temperature distribution. According to [29], the temperature of the Banda Sea thermocline layer during the southeast monsoon season is 17.09–23°C, while the average temperature distribution in this study is quite well distributed with a range of 16.6–17.2°C, and in the Banda Arc the temperature is warmer, namely 17.5–17.8°C.

To visualise the temperature variance in the Banda Sea, **Fig**. **4(b)** uses the same three layers as the average temperature distribution in **Fig. 4(a)**. Among the three layers, the surface layer displays high variance values (0.5–4°C^2) in NBS but does not exhibit distinct groupings like the other two layers. This indicates that the surface temperature is highly variable owing to the influence of the wind and waves. The coastal area has the highest variance, which could be due to the influence of local factors, such as land-sea interactions or coastal upwelling. In the near-surface layer, the variance value was the highest (1–5°C^2), forming three variance groups in the arc or east part (highest), west, and south (lowest) regions. This suggests that the temperature gradient is clearer in the near-surface layer because of the thermocline. Unlike the two layers preceding it, the thermocline layer exhibits a variance value ranging from 0.5°C^2 to 2°C^2 and comprises four variances: the highest in the southeast, followed by the south, northwest, southwest, and north (lowest). It acts as a

transition layer between the warmer mixed water at the surface and cooler deep water below. Temperature, salinity, and wind mixing influence depth and strength.

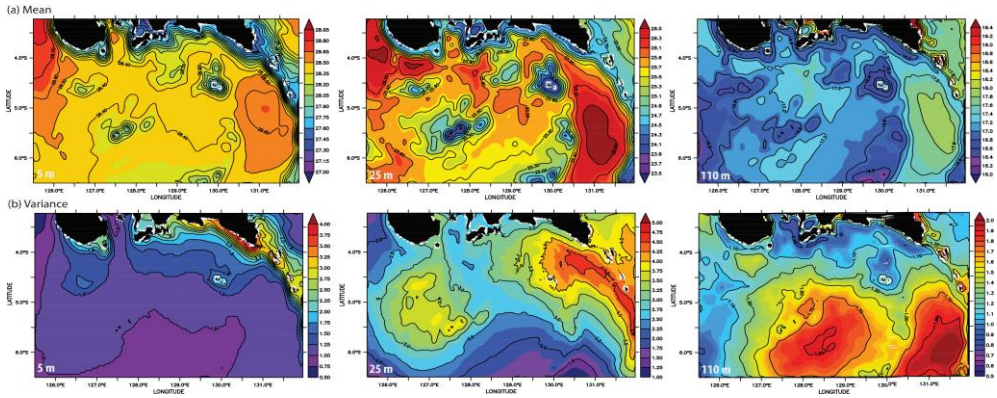

Fig. 4. Mean (a) and variance (b) of temperature at the surface (left), near-surface (middle), and thermocline layer (right) in the NBS from 2015 to 2022.

Fig. 5 shows the mean and variance of the salinity of the three layers of marine water, namely, the surface, near-surface, and thermocline layers in the NBS. **Fig. 5a** for the range of mean salinity values to 34–34.48 psu for the near-surface layer, 34.5–34.78 psu for the surface layer, 34.7–34.98 psu for the thermocline layer. In the surface layer, the salinity of the Banda Sea is highest around the island or coastal area and decreases towards the southwest, with salinity reaching 34.3 psu. In contrast to the surface layer, the near-surface layer of the Banda Sea is the highest outside the Banda Arc (northeast) at 34.77 psu, while the lowest salinity is in the Banda Arc, reaching 34.52 psu. The same range of values was also found in the northwest, whereas in the south, the salinity was distributed with a value of 34.62 psu. The NBS has salinity values in the thermocline layer that are evenly distributed, with the northeast having the highest salinity at almost 35 psu, whereas the southwest to the south has the lowest salinity value, reaching 34.71 psu. Total salinity ranged from 34.74 to 34.8 psu.

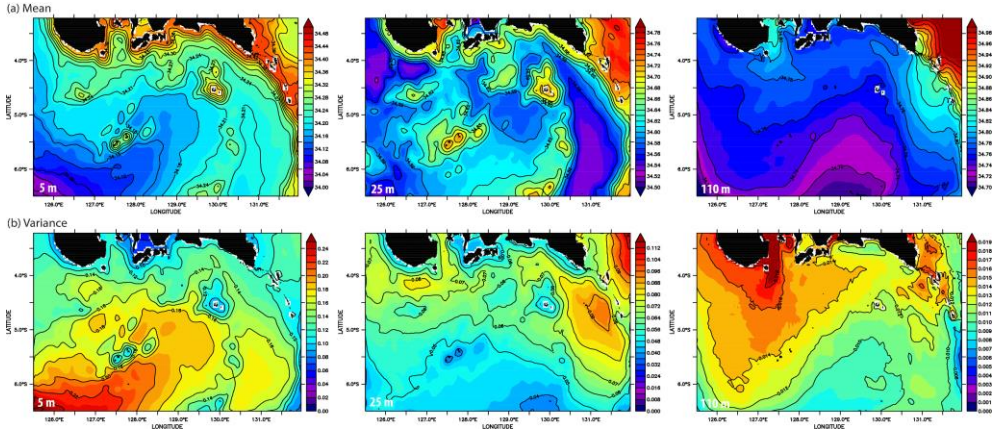

Fig. 5. Mean (a) and variance (b) of salinity at the surface (left), near-surface (middle), and thermocline layer (right) in the NBS from 2015 to 2022.

Fig. 5b illustrates the variance in salinity in the North Banda Sea with layers, as shown in **Fig. 5a**. Each layer has a different range of values. The surface layer has a variance value

range of 0-0.24 psu^2, with the highest value distributed in the southwest and then decreasing towards the coastal area. While the near-surface layer with a value range of 0-0.112 psu^2 is seen to form a difference at the top and bottom, at the bottom (south) the variance value is lower, reaching 0.04 psu^2, while the highest is at the top (to the northeast), reaching 0.112 psu^2. In contrast, the thermocline layer formed a different variance value with a range of 0.004-0.019 psu^2, where the distribution of the highest variance value was from the Manipa Strait and northwest to the offshore part of the Banda Sea. This suggests that the thermocline is clearer in this area, which could be due to factors such as seasonal weather variations, tides, and Indonesian Throughflow. In addition, the smallest variance group was formed in the east, with a value of 0.004 psu^2.

Fig. 6 shows the mean and variance of the eddy kinetic energy (EKE) in the NBS for the surface, near-surface, and thermocline layers. **Fig. 6a** shows the results of analysing the mean value of EKE with a range of values from 0-0.270 cm^2/s^2 in the surface layer, 0-0.255 cm^2/s^2 in the near-surface layer, and 0-0.240 cm^2/s^2 in the thermocline layer. The surface layer had a higher mean value than that of the other layers. As the mean EKE value decreased, the highest variance values formed clusters in the Manipa Strait in all three ocean layers, where these high clusters formed a constant decreasing cluster pattern from the Manipa Strait and northwest to southwest and south. Meanwhile, smaller mean EKE values were observed in the east and southeast. This is clearly visible in the thermocline layer. The mean value of the EKE in **Fig. 7a** is overlaid with the current vector. The current originating from the Manipa Strait first flows into the Banda Sea before dividing westward into the Banda Sea, where it joins the current from west of Buru Island, and eastward into the outer Banda Arc, where the current from east of Seram Island also enters the Banda Arc. A counterclockwise eddy is present in the thermocline layer, which is linked to currents entering the Banda Sea from the Manipa Strait.

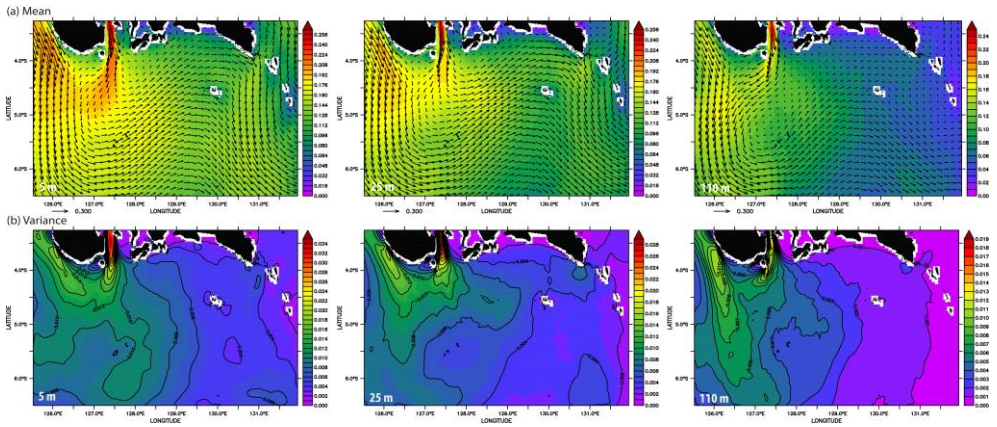

Fig. 6. Mean (a) and variance (b) of EKE at the surface (left), near-surface (middle), and thermocline layers (right) in the NBS from 2015 to 2022.

Additionally, **Fig. 6b** shows the variance values for the three layers, as shown in **Fig. 6a**. The EKE variance values exhibit a high variance group in the Manipa Strait with ranges of 0.024–0.034 (surface), 0.020–0.028 cm^2/s^2 (near-surface), and 0.011–0.014 (thermocline layer), similar to the EKE mean value group pattern. The variance value group formed in the entire western region is a medium group in all layers, whereas the eastern part forms the lowest variance group. The variance group of the thermocline layer differed significantly between the western and eastern regions of the research area. Notably, the variance value was zero in the eastern region. The difference in variance values can be attributed to the influence of the Manipa Strait, which acts as a barrier to the eastward flow of the NBS, resulting in a

reduction in EKE in the eastern part of the study area. The topography and sea depth of the Banda region may also have contributed to this effect.

3.3 Oceanic variability

Fig. 7 displays the NBS temperature time series and PSD for the period 2015–2022. The surface temperature, as presented in **Fig. 7a**, shows that the lowest temperature occurs in July 2015 and 2019, or the eastern season, which is approximately 25°C, while the highest sea surface temperature occurs in December 2020, or the western season, which is >30°C. Both El Niño and a positive IOD occurred in 2015 and 2019, impacting the surface layer. The significant Banda SST signal is influenced by both seasonal winds and ENSO-IOD phenomena. The periodicity of the significant NBS surface temperature signal was characterised by both annual and intraseasonal components, as demonstrated by the respective first and second highest peaks in the PSD analysis. Unlike the surface layer, the near-surface layer reveals the strongest periodicity of annual and interannual signals, which are characterised by annual variability in ocean temperatures. As shown in **Fig. 7b**, the lowest near-surface temperatures, which were 21.5°C in August 2015 and 22.2°C in August 2019, both coincided with the eastern monsoon. Meanwhile, the highest temperature was 28.4°C in March 2021, the first transition season. **Fig. 7c** displays the temperatures within the thermocline layer, indicating a low of 15.1°C in August 2019 and a high of 20.4°C. This layer has a significant interannual period.

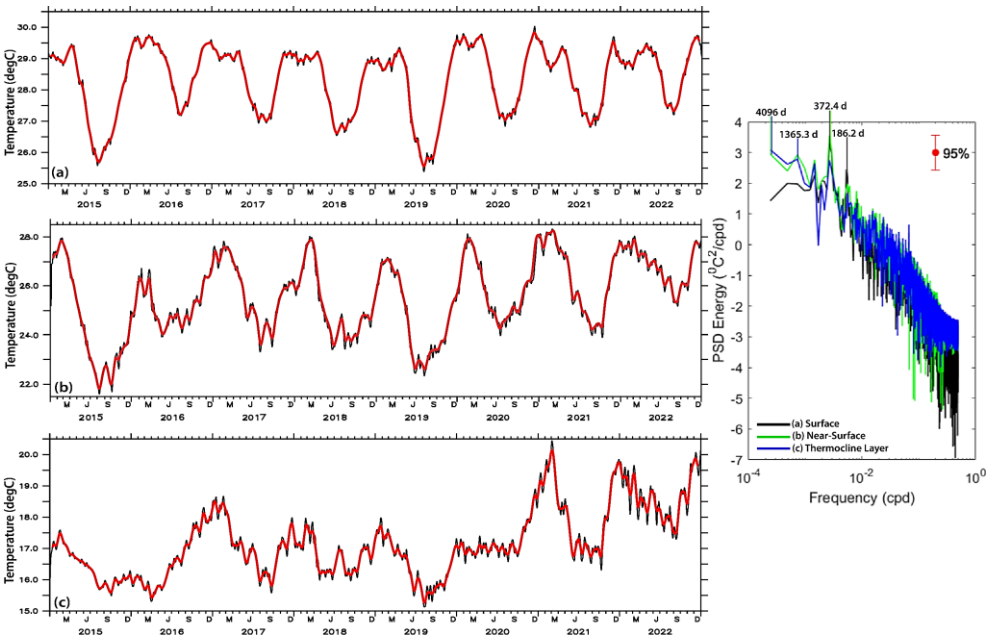

Fig. 7. Temperature Variability and Its PSD analysis at the surface (a), near-surface (b), and thermocline layers (c).

The salinity variability is demonstrated in the time series and PSD in **Fig. 8**. The salinity of the north Banda Sea surface (**Fig. 8a**) hit its lowest level during the first transition season, April 2019, with a value of 33.1 psu, whereas the saltiest salinity was at the end of the eastern season (August 2022), with a value of 34.9 psu. The significant signal of the Banda Sea surface salinity showed an annual period, and there was also an interannual signal. In **Fig. 8b**, the near-surface layer has its lowest salinity at the beginning of the first transitional

season, March 2018, at 33.9 psu, while the saltiest is at the beginning of the western season, December 2022, with salinity values reaching 35.1 psu. The salinity of this layer has the most significant interannual signal periodicity compared with the annual periodicity. As the water column becomes deeper, the salinity increases because in the thermocline layer in the same season (March 2018), the salinity reached 34.55 psu (the lowest in the thermocline layer). Conversely, the highest salinity value of 34.97 psu was recorded in May 2015 (**Fig. 8c**). While the surface and near-surface layers show annual signals, the salinity in the thermocline layer shows only the most significant interannual signal.

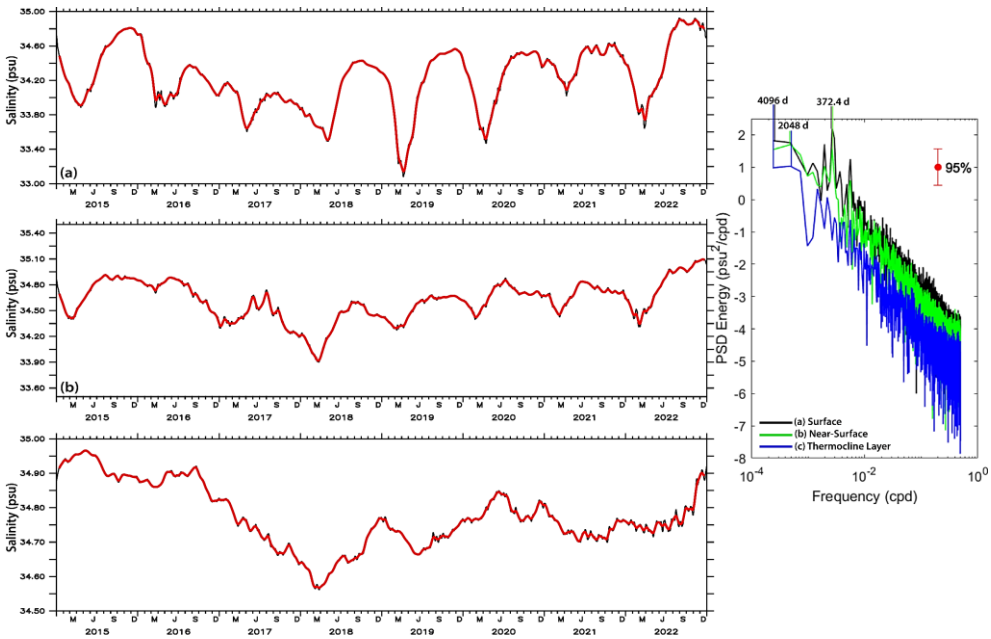

Fig. 8. Salinity Variability and Its PSD analysis at the surface (a), near-surface (b), and thermocline layers (c).

The time series and PSD of the zonal current velocities in the NBS are shown in **Fig. 9**. The zonal currents at the surface (**Fig. 9a**) are strongest compared to the near-surface and thermocline layers, reaching 0.5 m/s flowing eastward in February 2022 and 0.3 m/s flowing westward in August 2017. The dominant zonal current velocity in the surface layer displays annual and interannual periodicity. In May 2019, strong current velocities flowed eastward at >0.25 m/s and westward at 0.17 m/s in October 2022, while in the near-surface layer, the periodicity of zonal currents at near-surface depths is intraseasonal, according to the results of PSD analysis. Similar to the near-surface layer, the zonal current velocity in the thermocline layer peaked at 0.24 m/s eastward in September 2022, while the westward flow was 0.15 m/s in October 2022. However, the periodicity of the strongest zonal currents in the thermocline layer is annual and intraseasonal.

Fig. 10 displays the time series and PSD of the meridional current velocities in the NBS from three layers: surface, near-surface, and thermocline. The meridional currents in **Fig. 10a** indicate the strongest northward velocity of 0.17 m/s in December 2015 and March 2019, and a southward flow of 0.28 m/s in September 2021. The surface layer has meridional currents with significant periodicity, which occur on an annual and interannual basis. In the near-surface layer, the northward flow reached its maximum strength of 0.04 m/s in January 2016, while the southward flow was stronger at 0.19 m/s in December 2020. According to the PSD analysis, the meridional currents in the near-surface layer exhibit significant annual

and interannual periodicity, unlike those in the surface layer. The meridional current flowing northward experiences weakening in the thermocline layer, with December 2015 recording the strongest at 0.02 m/s, whereas the strongest southward flow appears in December 2020 at 0.11 m/s. The interannual and intraseasonal signals exhibited the highest periodicity in the thermocline layer.

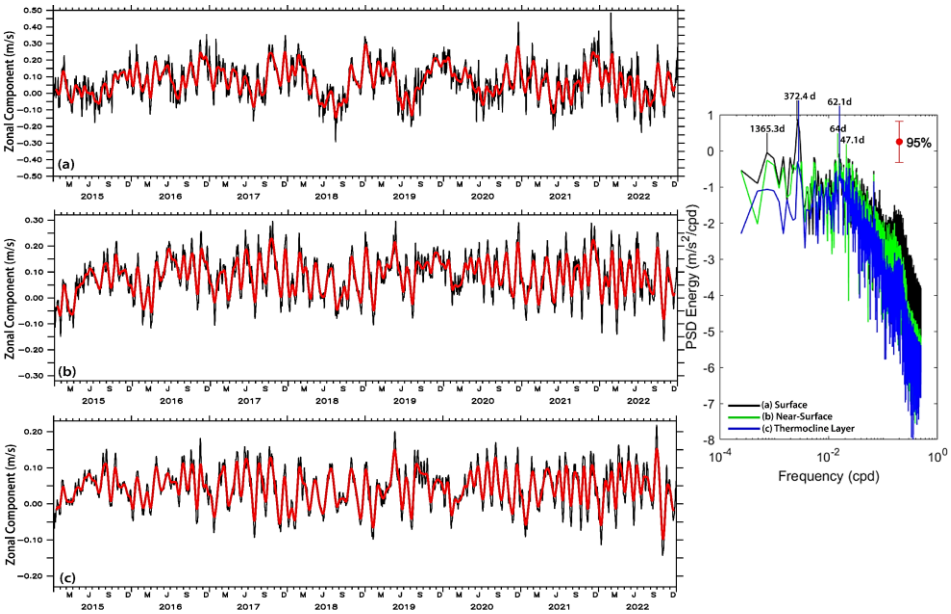

Fig. 9. Zonal Component Variability and Its PSD analysis at the surface (a), near-surface (b), and thermocline layer (c).

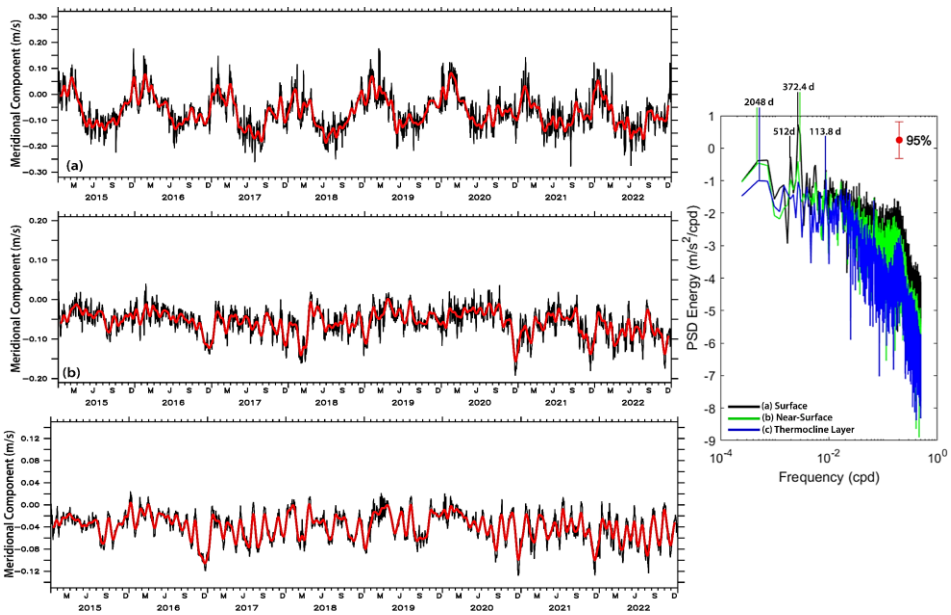

Fig. 10. Meridional Component Variability and Its PSD analysis at the surface (a), near-surface (b), and thermocline layer (c).

3.4 Hovmoller analysis of temperature and salinity

Fig. 11 shows a Hovmoller diagram illustrating the layers of ocean water: surface, near-surface, and thermocline layers along the horizontal transect of the dashed red line (**Fig. 1**). The diagram shows a consistent trend between 2015 and 2022 along the transect, with sea surface temperatures peaking at 30°C during the northwest monsoon season. The highest temperatures are more frequently observed between 131-131.5E or in the outer region of the Banda Sea arc. The same phenomenon was observed at transects 126–127E in both 2016 and 2020. Within the transect around 131.9E, the sea surface temperature decreased with the onset of the southeast monsoon season, with the lowest temperature of 24°C in 2015 and 2019. The fluctuation in temperature values in the Banda Sea indicates an annual periodicity of the Banda Sea surface temperature.

The near-surface layer and surface layer of the Banda Sea have the same annual temperature fluctuation pattern as the surface layer, with temperatures ranging from to 20-30°C. In contrast to the previous two layers, the thermocline layer had temperature characteristics with a dominant interannual periodicity. Owing to the La Niña phenomenon [30] in 2021/2022, the thermocline layer of the Banda Sea has become warmer than in previous years. During the eastern season, the thermocline layer is cooler because the southeast monsoon winds are stronger than those during the reverse season. The strong winds generate stronger waves and currents, which then drive the water mass in the ocean water column, causing the mixed layer to deepen and the thermocline layer to decrease; thus, the temperature is also colder than in the western season.

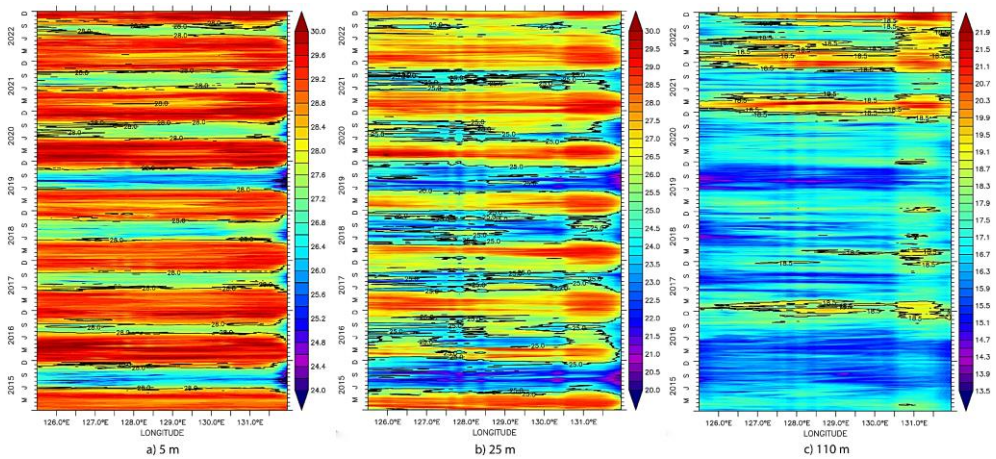

Fig. 11. Hovmoller Analysis of Sea Temperature at the surface (a), near-surface (b), and thermocline layer (c).

3.5 Interannual variations in oceanographic parameters related to ENSO and IOD

The time series of the standardised Southern Oscillation Index (SOI) obtained from [30] shows the ENSO and IOD phenomena that emerged between 2015-2022 (**Fig. 12a-b**). Negative anomalies (blue) indicate El Niño and negative IOD phenomena, while positive anomalies (red) of the SOI and DMI indicate La Niña and positive IOD phenomena. During this period, there was a strong El Niño in 2015/2016, negative IOD in 2018 and 2022, La Niña in 2017, positive IOD in 2018/2019, and strong La Niña in 2020-2022.

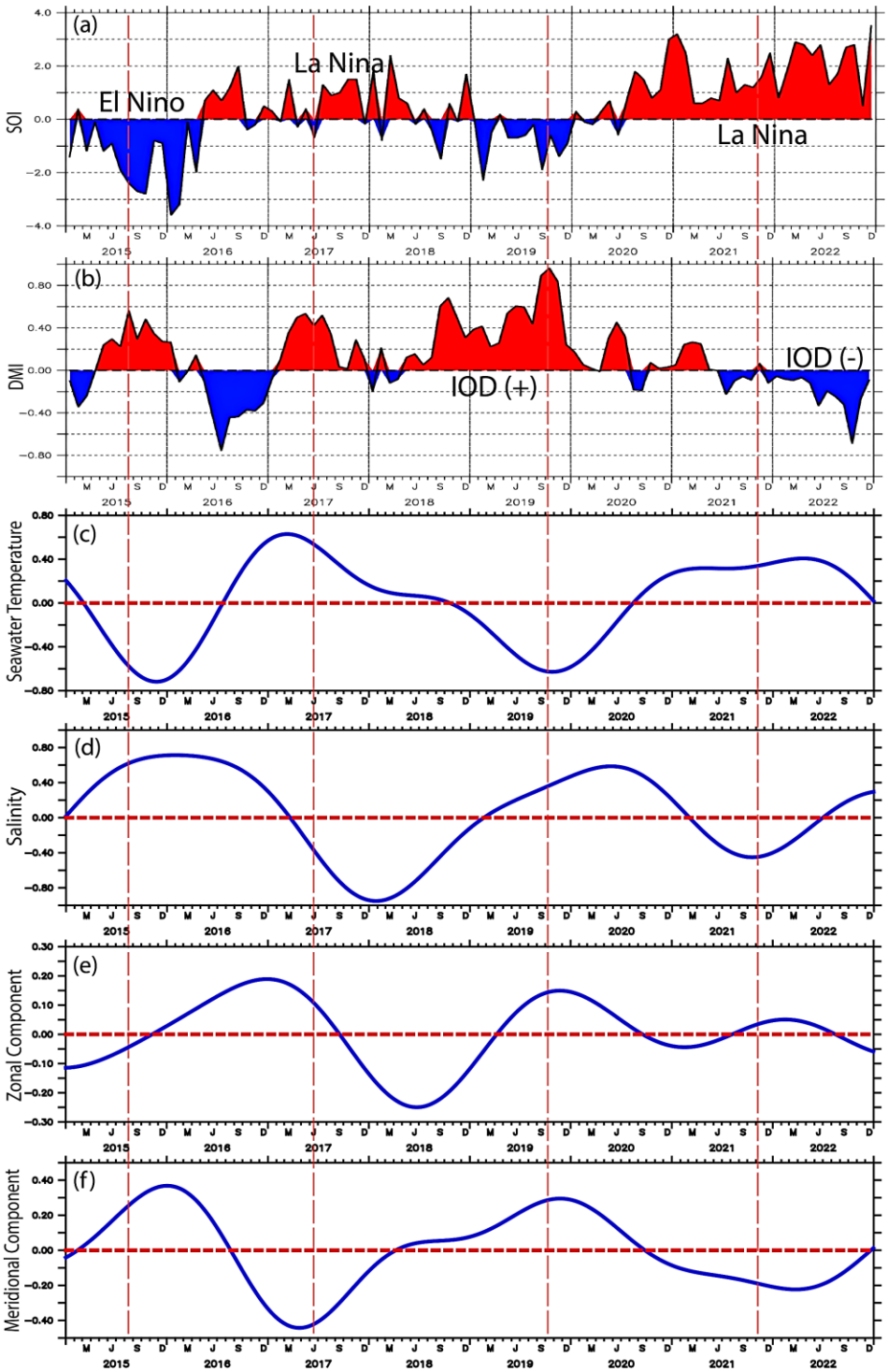

Fig. 12. Time series of ENSO indices (represented by SOI, a) and IOD indices (represented by DMI, b) and anomalies of ocean variables (c-g) in NBS. Note: Daily ocean variables (c-g) were removed from the annual mean.

The time series of the thermocline layer oceanographic parameter anomalies between 2015 and 2022 are shown in **Fig. 12 (c-f)**. These parameters clearly indicate the interannual variability associated with ENSO and IOD (**Fig. 12a–b**), indicating several major phenomena such as El Niño 2015, La Niña 2017, positive IOD 2018–2020, and La Niña 2020–2022. Strong El Niño peaks in 2015, La Niña in 2017, strong positive IOD in 2019, and strong La Niña in 2022. The oceanographic parameter anomalies are shown in **Fig. 12 (c-f)**, with annual averages omitted to obtain a better understanding of the variability between years.

The oceanographic parameters in the thermocline layer displayed variability between years, where seawater temperature and zonal current components were negatively correlated, whereas salinity and meridional current components were positively correlated with SOI and DMI, where El Niño and positive IOD occurred in 2015. The meridional component (**Fig. 12f**) shows positive and negative anomalies during El Niño (La Niña). Negative ocean temperature anomalies occurred during the strong positive IOD in 2019, when the zonal and meridional components of the current had high positive anomalies.

The western Pacific surface temperature plays a role in controlling the monsoon, with lower (higher) surface temperatures during El Niño (La Niña) years leading to stronger monsoons [32]. A stronger southeast monsoon causes stronger southeast winds in the study area. Southeast winds result in a reduction (increase) in wind stress during La Niña (El Niño) events, as indicated by the meridional component anomaly. During El Niño (La Niña), there were negative (positive) anomalies in the seawater temperature of the thermocline layer. Larger anomalies were observed during El Niño 2015. The increased meridional component during El Niño results in larger northward meridional currents, as indicated by the positive anomaly during El Niño 2015, which is much stronger than the negative anomaly during strong La Niña in 2022.

4 Conclusion

The CROCO 1/24º simulation results effectively validated satellite observations in the surface layer at locations representative of the Northern Banda Sea research area. Therefore, the data can be further analysed. Upon overlaying the model data, it became apparent that the differences below the surface layer can be attributed to the inherent limitations of the model configuration at the CTD coordinates. This observation highlights the need for a more precise and accurate model configuration in order to achieve a more comprehensive understanding. Additionally, the values and distribution of oceanographic parameters were affected by topography and depth. The fluctuations in multiple oceanographic parameters demonstrate the impact of monsoon winds, particularly in the surface and near-surface layers.

Our study shows the time series of SOI and oceanographic parameters between 2015 and 2022 and their association with El Niño and Indian Ocean Dipole (IOD) phenomena. The oceanographic parameters in the thermocline layer display interannual variability linked to ENSO and IOD, with notable peaks during El Niño in 2015, La Niña in 2017, a positive IOD in 2019, and La Niña in 2022. The temperature and zonal current components exhibited a negative correlation, whereas the salinity and meridional current components displayed a positive correlation with the SOI and DMI. Fluctuations in surface temperatures in the western Pacific have substantial effects on monsoon intensity, resulting in more robust monsoons during La Niña years.

The authors would like to thank E.U. Copernicus Marine Service Information for ocean–atmosphere data. CROCO and CROCO_TOOLS were obtained from https://www.croco-ocean.org. The authors are also grateful to the National Research and Innovation Agency of Indonesia for collecting and providing the oceanographic observation data. The authors thank the reviewers for their constructive feedback, which has greatly improved the manuscript.

References

1. E. Aldrian, *Meteorologi Laut Indonesia* (Badan Meteorologi dan Geofisika, Jakarta, 2008)
2. G.R. McGregor, S. Nieuwolt, *Tropical Climatology* (1998)
3. M.L. Shelton, *Hydroclimatology: Perspectives dan Applications* (Cambridge University Press, New York, 2009)
4. K.E. Trenberth, J. M Caron, J. Clim **13**, 4358 – 4365 (2000)
5. K. Wyrtki, *Report Scripps Inst. of Oceanography*, **2**, 42 (1961)
6. A.S. Atmadipoera, A. Koch-Larrouy, G. Madec, J. Grelet, F. Baurand, I. Jaya, I. Dadou, Deep Sea Res. 1 Oceanogr. Res. Pap., **182**, 103375 (2022)
7. W. Hutahaen, R.E. Wilson, Mar. Res. Indones., **28**, 81-95 (1992)
8. A.L. Gordon, *Oceanography*, **18**, 14-27 (2005)
9. B. Sukresno, I.W. Kasa, Ecotrophic, **3**, 87-91 (2008)
10. T. Shinoda, W. Han, E.J. Metzger, H.E. Hurlburt, J. Phys. Oceanogr, **42**,1099–1123 (2012)
11. R.D. Susanto, A.L. Gordon, Q. Zheng, J. Geophys. Res. Lett., **28**, 1599-1602 (2001)
12. U.O. Nurafifah, M. Zainuri, A. Wirasatriya, IJOCE, **4**, 74-85 (2022)
13. L.O.M. Giu, A.S. Atmadipoera, Y. Naulita, D.Y. Nugroho, J. Ilmu Teknol. Kelaut. Tropis, **12**, 457-472 (2020)
14. S.M. Horhoruw, M. Fadli, A.S. Atmadipoera, J. Lekalette, D.Y. Nugroho, W.M. Tatipatta, F. Kainama, *IOP Conf. Ser. Earth Environ. Sci.*, **618** (2020)
15. V.C. Masoleh, A.S. Atmadipoera, M. Purba, *IOP Conf. Ser. Earth Environ. Sci.*, **278** (2019)
16. S.M. Horhoruw, A.S. Atmadipoera, P. Nanlohy, I.W. Nurjaya, *IOP Conf. Ser. Earth Environ. Sci.*, **54** (2017)
17. H. Ratnawati, R. Hidayat, T. Juni, Omni-Akuatika, **12**, 119-130 (2016)
18. P. Weatherall, K. Marks, M. Jakobsson, T. Schmitt, S. Tani, J.E. Arndt, M. Rovere, D. Chayes, V. Ferrini, R. Wigney, Earth Space Sci., **2**, 331–345 (2015)
19. A.M.F. Ismail, J. Ribbe, Estuar. Coast. Shelf Sci., **227**, 106314 (2019)
20. P. Penven, P. Marchesiello, L. Debreu, J. Lefèvre, Environ. Model. Soft., **23**, 660-662 (2008)
21. G.D. Egbert,S.Y. Erofeeva, J. Atmos. Ocean. Technol., **19**, 183–204 (2002)
22. J-M. Lellouche, Le Galloude, E. Greiner, G. Garric, C. Regnier, M. Drevillon, R. Bourdalle-Badie, C. Bricaud, Y. Drillet, P-Y. Le Traon, Geophys. Res. Abs., **20**, 19806 (2018)
23. H. Hersbach, B. Bell, P. Berrisford, S. Hirahara, A. Horanyi, J. Munoz-Sabater, J. Nicolas, C. Peubey, R. Radu, D. Schepers, *et al*, Q.J.R. Meteorol. Soc., **46**, 1999–2049 (2020)
24. E. Hovmöller, Tellus, **1(2)**, 62-66 (1949)
25. W.J. Emery, R.E. Thomson, *Data analysis methods in physical oceanography* (Elsevier Science, 2014)
26. J.S. Bendat, A.G. Piersol, *Random Data: Analysis and Measurement Procedures*, (1971)
27. K.E. Taylor, J. Geophys. Res., **106**, 7183–7192 (2001)
28. A.A. Fahrezi, E.P. Wulandari, M. Arrafi, R. Ridwana, S. Himaya, Ilmu Kelaut.: Indones. J. Mar. Sci., **15**, 81–90 (2022)
29. D.D. Awayal, S. Tubalawony, Y.A. Noya, JFMR, **7**, 30-42 (2023)
30. NOAA National Centers for Environmental Information Climate Monitoring Southern Oscillation Index https://www.cpc.ncep.noaa.gov/ (2023)
31. NOAA Physical Sciences Laboratory, https://psl.noaa.gov/ (2023)

32. S. Steinke, M. Prange, C. Feist, J. Groeneveld, M. Mohtadi, J. Geophys. Res. Lett. **41**, 7684–7693 (2014)
33. M. Wang, B.Y. Dua, X. Qiu, Y. Cheng, X. Luo, Chen, M. Feng, J. Geophys. Res. Oceans, **122** (2017)